



OPEN Geological inference of channel and polka-dot seismic anomalies in Yeongil bay, Pohang

Min Je Lee¹, Gi-Bom Kim², Jiho Ha³, Yi Shen⁴ & Yongchae Cho^{1,5}✉

The Engineering Ocean Seismic 3D system, which enables ultra-high-resolution seismic surveys on a smaller survey scale, was deployed in Yeongil Bay, Pohang, South Korea. The region is renowned for abundant shallow gas deposits and faults. Based on acoustic impedance contrast and abnormal behavior observations, two seismic anomalies termed channel and polka-dot anomalies have been identified in the seismic volume. Seismic attribute analysis based on the signal amplitude and structural characteristics reveals that these anomalies correspond to shallow biogenic gas deposits. Structural interpretation of the seismic volume revealed that the contractional deformation resulting from post-Miocene neotectonics has resulted in uplift and reverse faulting in the Pohang region, contributing to the formation of anomalies. The channel anomalies correspond to gas-saturated tidal channels that formed during eustatic sea-level changes in the post-Last Glacial Maximum period. The polka-dot anomalies are located in topographic lows and are overlain by neotectonic sediment. The different behaviors of these anomalies in a seismic volume can be attributed to the different thicknesses of overburden overlying each of the anomalies.

Keywords Seismic anomalies, Small-scale acquisition, Biogenic gas, Near-surface seismic

The East Sea (Sea of Japan), a back-arc basin formed by Cenozoic back-arc extension¹, has been one of the most intensively researched regions in the eastern Korean Peninsula due to its tectonic implications^{2–5} and presence of shallow gas deposits^{6–8}. The formation process of the East Sea can be divided into (1) a pull-apart opening phase from the late Oligocene to early Miocene, (2) a rotational opening phase with differential rotation of the Japanese Arc from the early to middle Miocene, (3) a back-arc closing stage starting in the late Miocene^{2,9–14}, and finally (4) a neotectonic regime from post-Miocene (c. 4 Ma) to present day^{15–18}. Despite the tectonic implications of the East Sea, most studies on the evolution of the East Sea and the neotectonic regime have been carried out in the Ulleung Basin^{2,19,20} or the Japanese Arc^{15,18}, and the understanding of Quaternary structures and their geological implications in the coastal region of the southeastern Korean Peninsula is relatively insufficient due to lack of 3D (three-dimensional) seismic data with promising quality and 3D interpretation of the region, respectively.

These problems can be attributed to the limitations of conventional three-dimensional (3D) marine seismic surveys: (1) the requirement for large-capacity seismic sources ranging up to several hundred hertz and (2) multichannel streamer systems with streamer lengths of a few hundred meters to a few kilometers. Furthermore, such an acquisition system is often unavailable in coastal regions where the water depth is too shallow and anthropogenic activities prevail. To mitigate these limitations, the Korea Institute of Geoscience and Mineral Resources (KIGAM) developed the Engineering Ocean Seismic 3D (EOS3D) project. This newly developed survey system enables small-vessel surveys by reducing the required number of personnel and the size of the equipment²¹.

Yeongil Bay, Pohang, South Korea, is located in the Pohang Basin, which is proximal to the eastern continental margin of the Korean Peninsula (Fig. 1). Due to its shallow bathymetry (approximately 50 meters)²² and because it is adjacent to one of the most populated ports in Korea, a conventional 3D seismic survey cannot be employed in Yeongil Bay. However, the small-scale seismic volume obtained by the EOS3D survey performed in Yeongil Bay revealed that the region contains features that can aid in the structural interpretation of the regional geology of the coastal region of the southeastern Korean Peninsula: seismic anomalies, shallow faults, reverse faults, etc.

¹Department of Energy Systems Engineering, Seoul National University, Seoul 08826, Republic of Korea.

²Department of Geological Sciences, Pusan National University, Busan 46241, Republic of Korea. ³Korea Institute of Geoscience and Mineral Resources, Pohang 37559, Republic of Korea. ⁴School of Geosciences, China University of Petroleum (East China), Qingdao 266580, China. ⁵Research Institute of Energy and Resources, Seoul National University, Seoul 08826, Republic of Korea. ✉email: yc.cho@snu.ac.kr

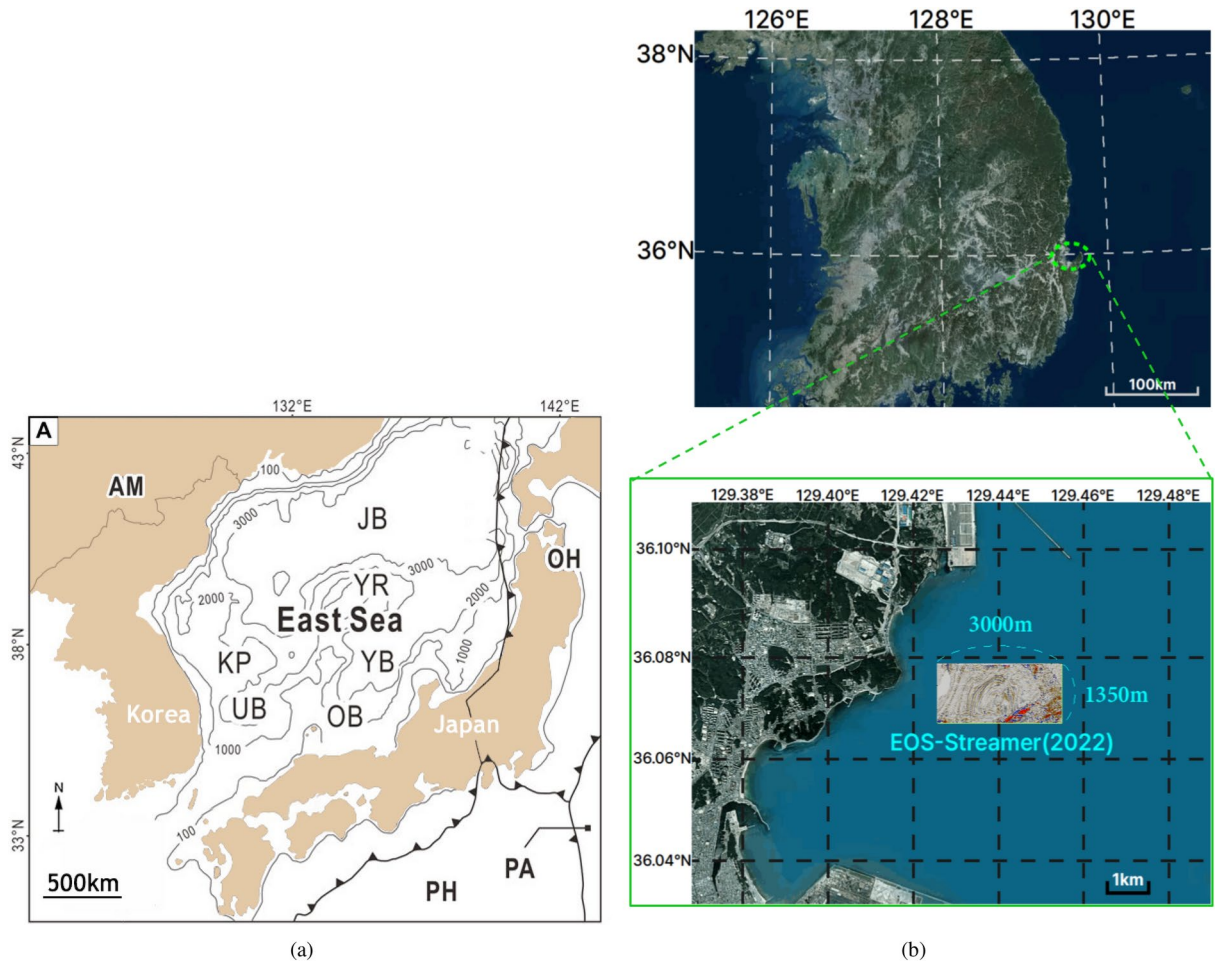


Figure 1. (a) Illustration of the bathymetric and tectonic context of the East Sea (modified after^{2,16}) and (b) Location of study area in southeastern Korea marked by green circle(top) and magnified satellite image with the seismic data(bottom). AM: Amur Plate, PA: Pacific Plate, PH: Philippine Sea Plate, OH: Okhotsk Plate, UB: Ulleung Basin, YB: Yamato Basin, JB: Japan Basin, YR: Yamato Rise, OB: Oki Bank, KP: Korea Plateau. This figure was generated using the Adobe Illustrator software (<https://www.adobe.com/products/illustrator.html>).

In hydrocarbon exploration, seismic anomalies often play a crucial role in identifying the structure of interest due to their distinct physical characteristics in seismic data²³. Seismic anomalies can be described as dramatic changes in seismic amplitude often resulting from changes in the relative acoustic impedance. Typical forms of seismic anomalies include but are not limited to bright spots, acoustic blanking, seismic chimneys, and pockmarks^{24–27}. Each of these anomalies can be used as a direct or indirect indication of the possible presence of hydrocarbon resources. Seismic anomalies can also help interpret the evolution of regional geology by providing valid reference points, such as relative time constraints, in the reconstruction.

Based on the 3D seismic volume obtained from the EOS system, this study aims to analyze the physical characteristics of the seismic anomalies, termed channel and polka-dot anomalies, present in the seismic volume. Furthermore, based on the seismic attribute analysis of said anomalies and the history of the regional geology of the East Sea, the interpretation of the coastal region of the southeastern Korean Peninsula is performed to specify the geological process that resulted in the formation of said anomalies in respect to the East Sea formation. In doing so, this study aims to provide a geological reference by the characterization of seismic anomalies in different regions in the world with similar physical behavior but also the comprehension of the East Sea formation and the neotectonic regime which has been identified as one of the major driving factors in the deformation of the East Sea and the southeastern Korean Peninsula to provide insight into the contractional deformation process of the post-rift back-arc formation.

Data acquisition

Acquisition area: Yeongil bay

The seismic data used in the study were acquired from Yeongil Bay near the Pohang Basin which is located in the southeastern Korean Peninsula. Figure 1 illustrates the location of the acquisition site in a satellite image. The survey geometry is 3,000 meters in the E-W direction and 1,350 meters in the N-W direction. The East Sea is well known for its abundant distribution of shallow faults and gas deposits^{2,8,28}, and the survey site was chosen

based on these characteristics, which were observed in previous surveys^{29,30}. Furthermore, this region is known to contain Miocene basins that developed as part of the western boundary fault system of the Ulleung Basin³¹. For these reasons, the region of study has been subjected to various geophysical surveys in recent years, with the objectives of hydrocarbon prospecting and identification of potential candidates for CO₂ sequestration.

The Pohang Basin is the largest Tertiary sedimentary basin on the Korean Peninsula, with the Miocene Yeonil Group being thickly distributed in the western part of Yeongil Bay with a maximum thickness of 900 m^{32,33}. This group mainly consists of sedimentary rocks, including conglomerates, sandstones, and mudstones deposited in several fan delta environments. In the eastern part of Yeongil Bay, Paleogene volcanic rocks and volcanoclastic rocks prevail³⁴. Furthermore, shallow faults and folds due to contractional deformation are abundant in the region of study.

EOS system

The Engineering Ocean Seismic 3D (EOS-3D) system, developed by KIGAM in 2014, has the fundamental objectives of operating small vessels with fewer crewmembers, optimizing surveys for other applications, and maximizing synergy with other survey equipment²¹. This survey system also enables 3D ultra-high-resolution (UHR) surveying, which is characterized by (1) a high-frequency (80–1000 Hz) band seismic source, (2) a minimized bin size (3.125 m or less in the inline direction) via reduced shooting intervals and receiver channel spacing, and (3) high-speed digital sampling recording highly precise seismic data²¹.

The EOS-Streamer system consists of a main controller, source system, receiver system, and global positioning system (GPS). The survey design used to acquire the seismic data in this study utilized four-line eight-channel streamers, which are compact and lightweight enough to be towed by 40-ton vessels. The brief survey procedure is as follows: (1) electrical signals are repeatedly sent out by an external trigger in the main controller; (2) the signals activate the seismic source underwater; (3) the seismic source generates seismic signals that are then scattered, reflected, and refracted in response to the subsurface geometry and physical properties; (4) the receiver system, consisting of multichannel streamers, converts these signals into electrical signals; and finally (5) once the electrical signals from seismic responses are converted into a digital format, the GPS information of the survey is combined to form standard seismic survey data in the SEG-Y format²¹.

Figure 2 shows a schematic diagram of the survey design. A single unit with a 10 in³ airgun source is towed underwater 15 meters behind the survey vessel. Four lines of eight-channel streamers with a channel spacing of 3.125 meters are used as receiver systems and are towed 5 meters behind the front buoy. The channel spacing between hydrophones is determined based on the structural stability of the fluid-filled streamer tubes, incoherent noise, and bulge waves³⁵. The front buoy is towed 20 meters behind the back of the vessel. The line spacing is set to 5 m, and to ensure the spacing between the lines, deflectors are attached next to the left and right front buoys. Precise coordinate information about the source and each streamer channel is one of the most crucial aspects of 3D seismic surveys. Therefore, a wired B-RTK GPS and a Wi-Fi-type wireless B-RTK GPS are attached to the source and receiver systems, respectively. Field data were acquired over a total of 19 days during three voyages (June, August, and October). The distance between neighboring survey lines was 10 meters. A specification of this survey is described in Table 1.

Methods

Data processing

Marine seismic survey data often suffer from signal contamination due to noise and other artifacts that hinder an accurate interpretation of the data³⁶. To eliminate unwanted aspects in the raw data and to enhance the data quality for accurate interpretation, a conventional seismic data processing workflow is applied to the acquired data^{35,37,38}. The processing workflow is divided into two major stages: individual trace processing and stacked cube generation.

First, the denoising technique is applied to suppress unwanted noise in the data. Such noise includes coherent noise and random noise. The former can be linearly removed since adjacent traces share a phase relationship. However, the latter lacks a phase relationship between adjacent traces and cannot be correlated to the seismic energy source. This type of noise can be suppressed by stacking the traces and filtering³⁷. In this study, a band-pass filter with a range of 80, 120, 800, and 1500 Hz was applied to the obtained seismic data in order to suppress noise³⁷.

After the noise is removed from the data, debubbling is applied to remove the bubbling effect from the gas bubbles produced by an airgun. These bubbles oscillate and produce subsequent pulses that result in source-generated noise. This process is carried out by performing source estimation in order to extract the waveform followed by deterministic deconvolution. After eliminating bubble effects from the extracted waveform, a convolution was applied to obtain de-bubbled data.

Additional conventional marine seismic data processing steps, such as sea-bottom picking and swell correction³⁹, are applied. The data are regrouped and sorted according to the common depth gather (CDP) and line. Afterward, the normal moveout correction is applied to remove the offset effect, which refers to the delay in the arrival time of a reflection caused by the offset between a source and a receiver system. Since the maximum offset of the data was insufficient to perform NMO correction, a traditional approach of identifying a point of maximum energy in a semblance panel was unavailable. Instead, a constant-velocity model of 1500 m/s and the actual shot-receiver offset were used to perform the NMO correction on the data⁴⁰. After this process, traces with larger offsets are stretched in a time-varying manner, causing their frequency content to shift toward the lower end of the spectrum.

Subsequently, the traces are stacked after normal moveout correction. This results in the enhancement of the signals and the suppression of random noise. To mitigate the problems associated with diffraction hyperbolas and false-reflector position, poststack Stolt migration was performed⁴¹. Furthermore, to minimize the multiple

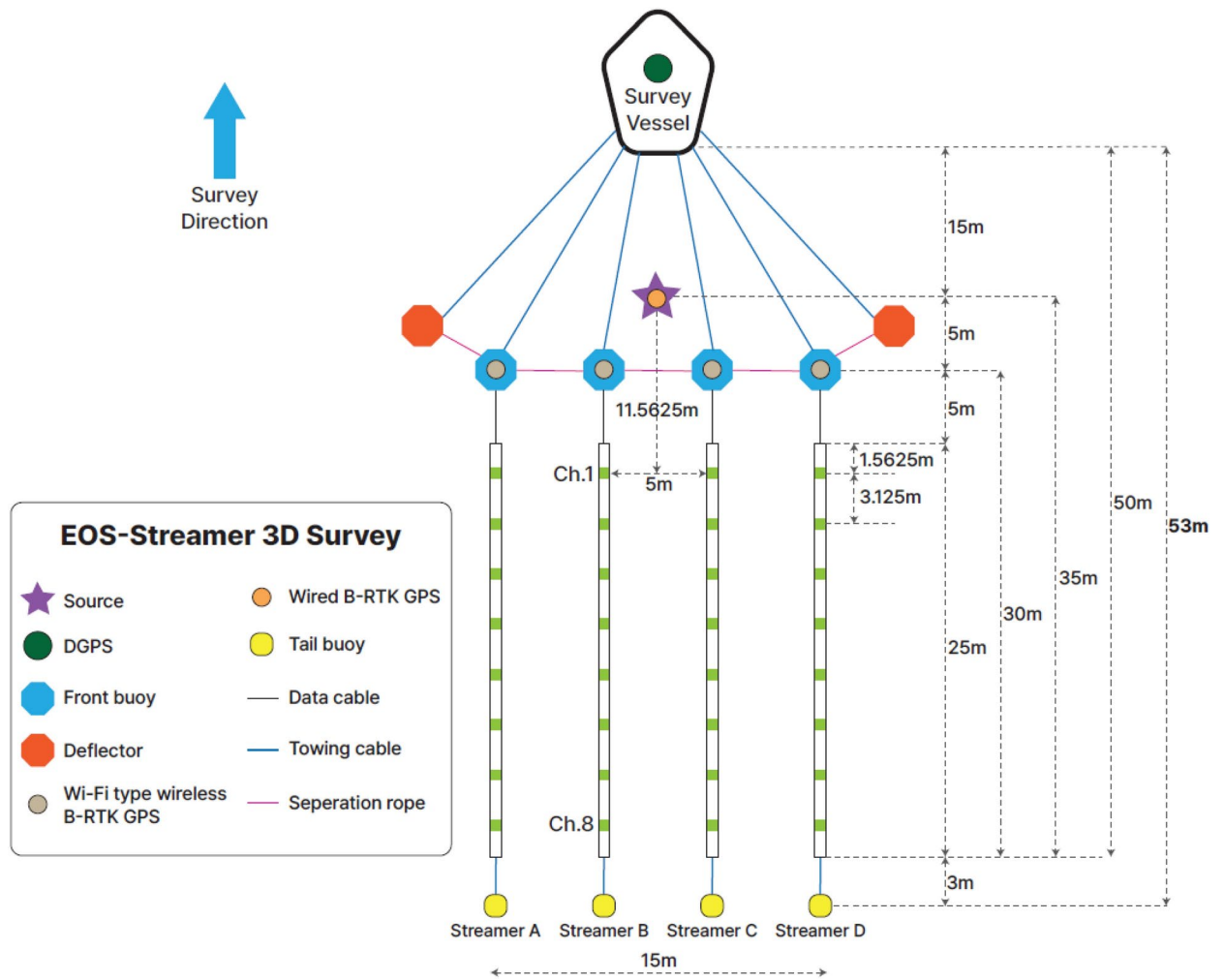


Figure 2. Illustration of the EOS-streamer operated on a 40-ton vessel with a single unit of 10 in³ airgun source. The specific survey design is shown in the figure. This figure was generated using the Adobe Illustrator software (<https://www.adobe.com/products/illustrator.html>).

EOS-Streamer Survey (2022) specification	
Parameter	Value
Survey date	Total 19 days in June, August, October, 2022
Location	Yeongil Bay, Pohang, South Korea
Source	10 in ³ single unit airgun (Bolt 2800LLX)
Source interval	2 Sec
Number of channels	32 channels (8 channels × 4 groups)
Channel interval	3.125 m in inline direction, 5 m in crossline direction
Sampling information	500 ms record length; 0.25 ms sample interval
Vessel weight	40 tons

Table 1. Specifications for EOS Streamer survey in 2022.

in the data, a predictive deconvolution was applied to the data⁴². 3D regularization is applied to each group of traces to produce a 3D volume cube for each group of traces. Finally, the generated 3D volume cubes are stacked into the final 3D volume cube used in this study. Figure 3 illustrates the workflow of the data processing sequence.

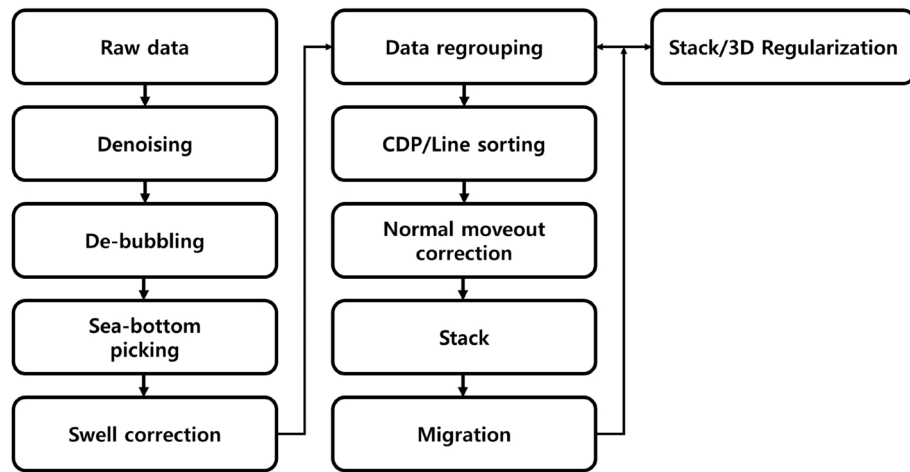


Figure 3. Workflow chart illustrating a marine data processing sequence applied to the acquired data in this study. This figure was generated using the Adobe Illustrator software (<https://www.adobe.com/products/illustrator.html>).

Seismic attributes

Evaluating seismic anomalies in plain seismic data is often problematic since the identification of anomalies heavily depends on the quality and clarity of the seismic data. To mitigate such limitations, in this study, seismic attributes are utilized. Seismic attributes can improve the results of seismic interpretation by revealing hidden features, identifying similar patterns, and quantifying specific properties^{43–45}. In other words, seismic attributes describe seismic data from different points of view according to the interpretation objective by decomposing the seismic data into attributes.

Seismic attributes record information from prestack and poststack data. Since the data already underwent a stacking process, poststack attributes are used in this study. Poststack attributes treat seismic data as images of the subsurface of the Earth. Among the countless seismic attributes considered in this study, several attributes are chosen based on their ability to highlight possible hydrocarbon deposits. The attributes are divided into two criteria based on their objective: geophysical and geological. The following section provides a conceptual explanation of seismic attributes.

Geophysical attributes

Geophysical attributes used in this study highlight the characteristics of the data itself, such as the amplitude, frequency, and phase.

Root-mean-square amplitude The root-mean-square (RMS) is the process of finding a representative value of a set of data values. The rms value x_{rms} of a seismic trace x_n with N samples is calculated as follows⁴⁶.

$$x_{rms} = \sqrt{\frac{1}{N} \sum_{n=1}^N x_n^2}$$

Similar to the average absolute value, the RMS value is independent of the sign of the data values. It computes the square root of the sum of squared amplitude values divided by the number of samples within the specified window size. The computed amplitudes are used as a simple means to identify possible hydrocarbon zones in the reconnaissance stage of seismic surveys⁴⁷.

Envelope The envelope is an amplitude measure that envelops the seismic trace. The envelope is a representation of the amplitude $E(t)$ of an oscillatory function $f(t)$. The envelope is independent of the phase or polarity. The envelope can be represented as a complex-valued function $S(t)$ as follows:

$$E(t) = \sqrt{(\text{Re}[S(t)])^2 + (\text{Im}[S(t)])^2}$$

where $\text{Re}[S(t)]$ represents the real part of the trace, which is essentially $f(t)$, and $\text{Im}[S(t)]$ is an imaginary part of the trace computed by taking the Hilbert transform of $\text{Re}[S(t)]$. The envelope is a physical attribute that can be used to identify bright spots, gas accumulation, major lithologic changes, sequence boundaries, etc.⁴⁸.

Sweetness Sweetness is a composite seismic attribute obtained by dividing the instantaneous amplitude (i.e., amplitude envelope) by the square root of the instantaneous frequency⁴⁹. Displaying the sweetness of the data reduces the contribution of high-frequency events. Regions of higher amplitudes and lower frequencies, such as sandy intervals, display the highest sweetness values. On the other hand, sediments with lower amplitudes and higher frequencies, such as thinly bedded shale, have lower sweetness values. This characteristic is particularly

advantageous when identifying gas reservoirs, hydrates, and salt bodies, which are examples of high-amplitude gas reservoirs.

Geological attributes

Unlike geophysical attributes, geological attributes used in this study highlight the structural aspects of the data, such as the dip, azimuth, curvature, and coherency. These attributes are particularly useful in analyzing the structure and geometry of the data⁴³.

Local structural dip The local structural dip is an edge detection method that highlights the rapid changes in local dips⁵⁰. In most cases, the areas of acoustic blanking and seismic chimneys exhibit severe variations in local dip values due to chaotic signals⁵¹.

Chaos The chaos attribute maps the chaoticness of a local seismic signal from a statistical analysis of dip/azimuth estimates⁵². This approach highlights the position of reflector distortion. This distortion may be due to various factors ranging from fractures to gas deposits. Chaos attributes are often utilized for identifying channel infill, gas chimneys, reef internal textures, sinkholes, salt diapirs, etc. In this study, chaos attributes are used to highlight the signal distortion beneath anomalies.

Variance Variance, also known as coherence, quantifies the discontinuity between neighboring signals. The local variance in the seismic data is computed by means of a predefined multiple-trace window⁵³. This attribute is amplitude invariant, which means that it produces the same response for the same seismic signature in both low- and high-amplitude regions. Topical subheadings are allowed. Authors must ensure that their Methods section includes adequate experimental and characterization data necessary for others in the field to reproduce their work.

Seismic data and anomalies

This section provides an overview of the 3D seismic data used in this study. The seismic data consists of 1200 inlines and 540 crosslines with a spacing of 3.125 m in the inline direction and 5 m in the crossline direction. The total recorded time length of the data is 500 ms, with a sampling interval of 0.25 milliseconds. To better illustrate the overall structure of the data, inline section 255 and crossline section 891 are shown in Fig. 4 and 5. Four seismic horizons (H1-4), including the seafloor (H1), and three seismic units (U1-3), are interpreted based on the most prominent reflectors in each sedimentary group with a uniform trend of deposition. As mentioned in the previous section, although the predictive deconvolution was applied, one may observe that the second multiple, indicated by a yellow box in Fig. 4 is not completely attenuated.

Between H3 and H4, U3 is present. This unit consists of continuous, parallel/subparallel strata. These strata are inclined in the western part of the volume, where they form a regional angular unconformity. In the eastern part of the volume, U3 has been deformed by folding and the east-dipping high-angle reverse fault (F1). The eastern

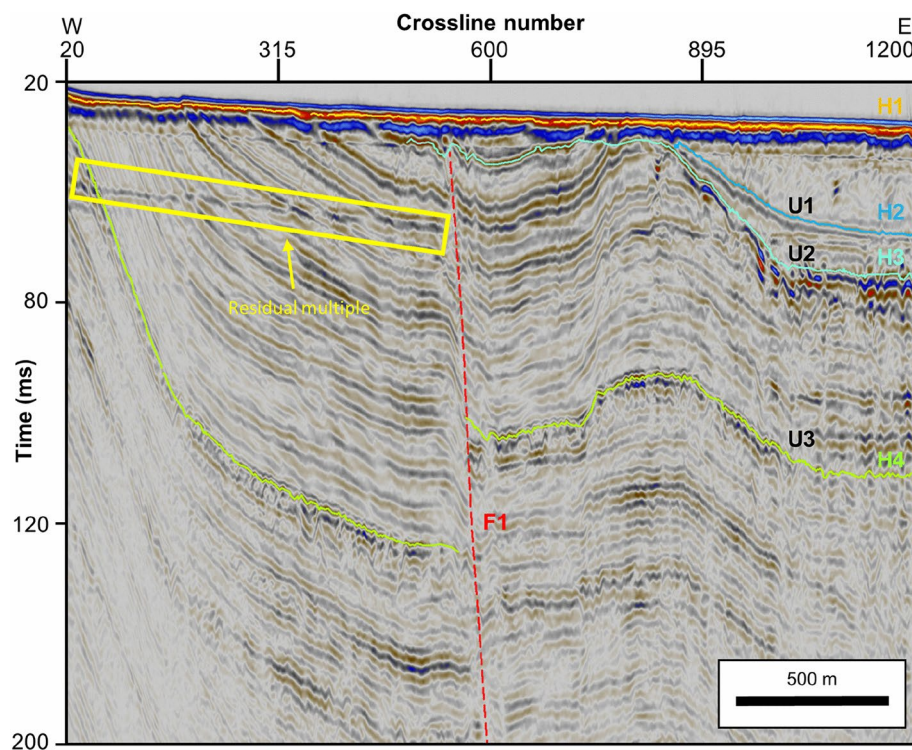


Figure 4. Illustration of interpreted seismic units (U1-3), horizons (H1-4), and fault (F1) in inline 255. The figure is vertically exaggerated by the factor of c.a. 6. Refer to Fig. 6 for location. This figure was generated using the Petrel software (<https://www.software.slb.com/products/petrel>).

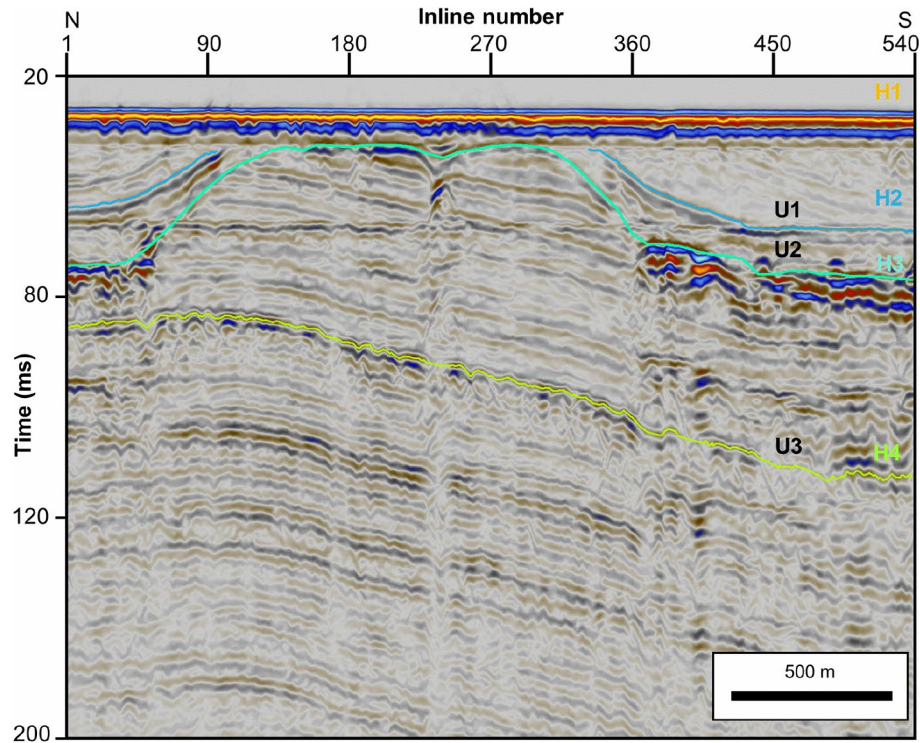


Figure 5. Illustration of interpreted seismic units (U1-3) and horizons (H1-4) in crossline 891. The figure is vertically exaggerated by the factor of c.a. 6. Refer to Fig. 6 for location. This figure was generated using the Petrel software (<https://www.software.slb.com/products/petrel>).

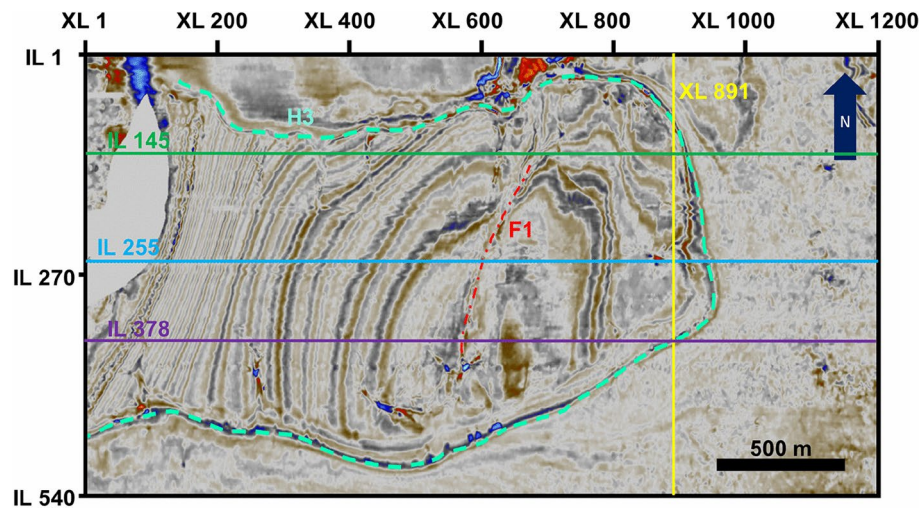


Figure 6. Timeslice at 45 ms indicating the location of inline 145 (green line), 255 (skyblue line), 378 (purple line) and crossline 891 (yellow line). Additionally, H3 (dashed coral-blue line) and F1 (dashed red line) are shown. This figure was generated using the Petrel software (<https://www.software.slb.com/products/petrel>).

limb of the fold shows truncational stratal termination resulting from slope failure. Above H3, U1 and U2 exhibit parallel depositional patterns that pinch out toward the west, which is characteristic of the syn-deformation sequence. Figure 6 shows that the strike of this reverse fault is NNE-SSW. Figure 6 also shows a boundary between the structural high and topographic low, indicated by H3 (dashed coral-blue line). The western part of the volume is a structural high resulting from the tectonic inversion process during the formation of the East Sea. The northern, southern, and eastern margins of the structural high are surrounded by post-neotectonic deposits that fill the topographic low. A temporal information on the stratigraphy is derived from the preceding research on the stratigraphy and formation of the East Sea and southeastern Korean Peninsula^{2,4,16,54}.

There are two major seismic anomalies in inline 145 and 378, respectively (Figs. 7, and 8, refer to Fig. 6 for location). Both anomalies exhibit typical characteristics of hydrocarbon presence such as acoustic impedance contrast, bright spots, velocity pull-downs, and phase reversals^{55–57}. However, the following observations of the anomalies describe rather unusual structural characteristics. The first anomaly, which is referred to as the “channel anomaly” in this study, is located between 25 and 45 ms in inline 145 (marked by red circles) in Fig. 7. Beneath the channel anomalies, there are regions of seismic signal distortion that extend to the bottom of the seismic section. On the top of this signal-distorted region, high-amplitude features exhibiting amplitude contrasts with the surroundings are present. Above these high-amplitude features, pockmarks are also visible in a yellow circle in Fig. 7. These anomalies have widths ranging from 15 to 30 m. Furthermore, although these anomalies exhibit narrower widths compared to typical channels visible in seismic data^{58,59}, they exhibit incised channel-like geometries when viewed in a timeslice (Fig. 9, red circles), which indicate paleochannels in the region; hence, the name “channel anomaly”.

The second seismic anomalies are mostly distributed among the topographic low in the seismic volume. These anomalies show clear features of bright spots, as indicated by the purple circle in Figs. 7 and 8. In inline 378, these anomalies show laterally distributed high amplitude contrasts that resemble the features of typical bright spots. Among these lateral bright spots, pillar-like structures, marked by red arrows in Fig. 8, are present. These pillars have widths ranging from 15 to 30 m. Figure 10 shows a timeslice at 71 ms; in this timeslice, these pillar-like structures exhibit droplet-like geometry with an amplitude contrast with the surroundings; hence, the name “polka-dot” anomaly (Fig. 10). Solely based on the structural characteristics, these anomalies resemble various seismic anomalies such as pinnacle reefs, dolines, and concretions^{60–65}. However, the identification of polka-dot anomalies based on attribute analysis will be provided in the later section.

In both channel and polka-dot anomalies, interesting characteristics can be observed which may indicate the presence of fluid. In Fig. 7, in the yellow circle indicating the channel anomaly, velocity pull-downs are visible. This behavior is consistent in the polka-dot anomalies in Fig. 8. Velocity pull-downs are caused due to the difference in the “path length” of a medium through which the seismic wave propagates. In this case, a pulled-down characteristic may indicate an underlying fluid (low-velocity zone) which allows the seismic wave to travel in longer path length^{55,56}. Another notable behavior is the phase reversal in the anomalies. In both channel and polka-dot anomalies, the phase in seismic data is reversed from positive to negative indicating an incidence of seismic wave from the higher acoustic impedance medium to the lower acoustic impedance medium⁵⁷ which is potential fluid saturated formation in this example⁴⁷.

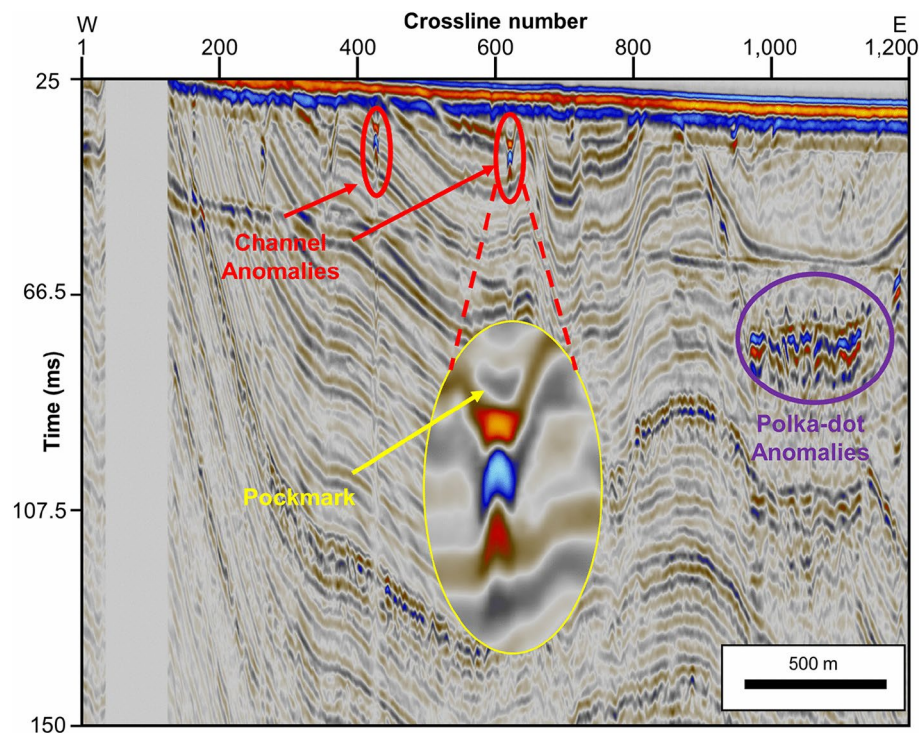


Figure 7. Inline section 145 showing anomalies; the red circle indicates channel anomalies and the purple circle indicates polka-dot anomalies. The yellow circle shows a magnified view of one of the channel anomalies and the yellow arrow points at the pockmark on top of the channel anomaly. The data gap in the left is due to the survey error. The figure is vertically exaggerated by the factor of 3.7. Refer to Fig. 6 for location. This figure was generated using the Petrel software (<https://www.software.slb.com/products/petrel>).

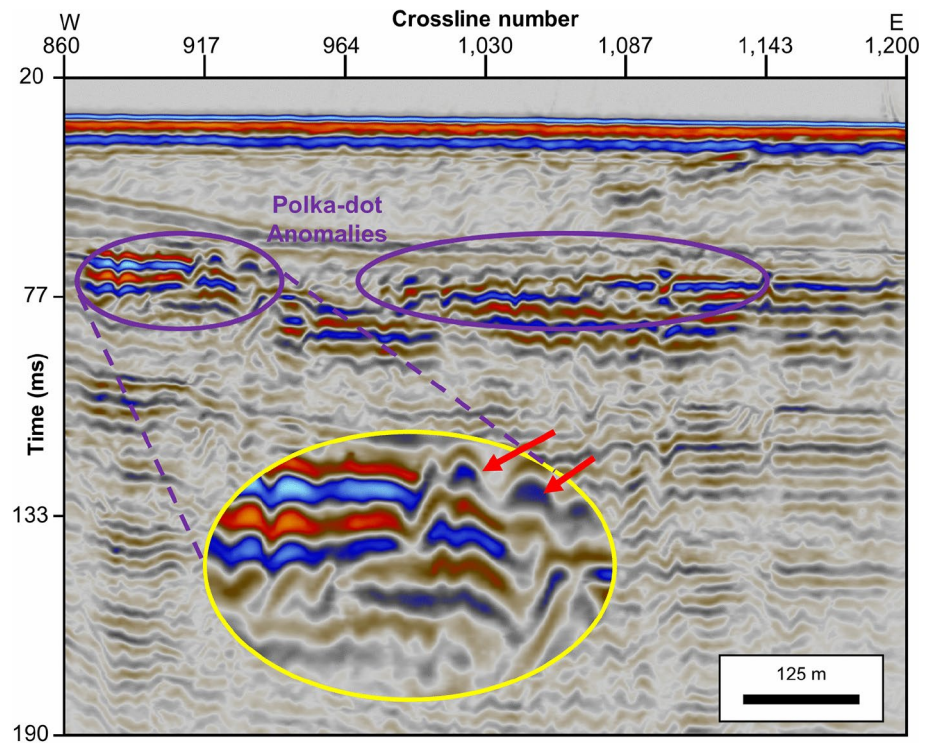


Figure 8. Inline section 378 showing polka-dot anomalies with evident bright spots marked by purple circles. The yellow circle shows a magnified view of the polka-dot anomalies. Red arrows are pointing at the pillar-like structures of the polka-dot anomalies. The figure is vertically exaggerated by the factor of 3.7. Refer to Fig. 6 for location. This figure was generated using the Petrel software (<https://www.software.slb.com/products/petrel>).

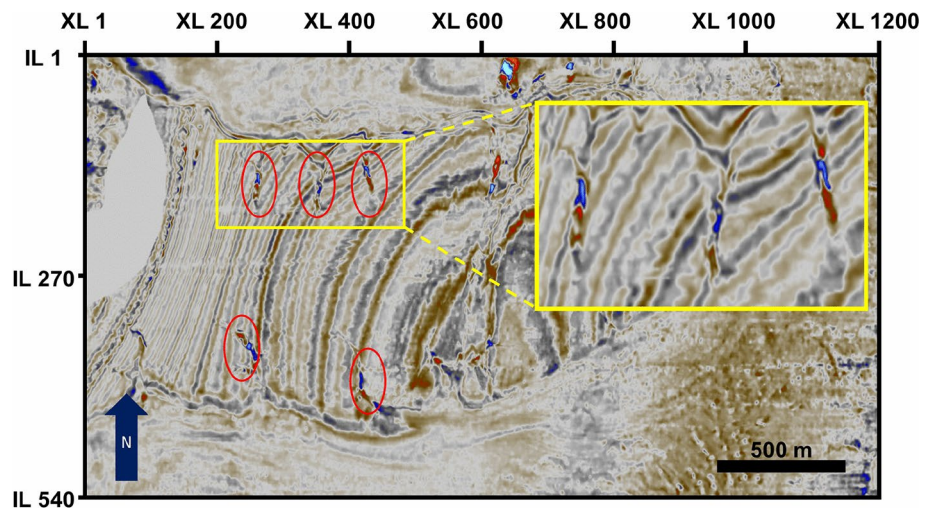


Figure 9. Timeslice at 39 ms; Illustration of “channel anomaly”. The yellow box marks a magnified view of channel anomalies. This figure was generated using the Petrel software (<https://www.software.slb.com/products/petrel>).

Results and discussion

Seismic attribute analysis

The channel anomalies show distinct features that are considered typical hydrocarbon indicators: bright spots, acoustic blanking, and pockmarks at the top^{47,66–68}. To further examine this anomaly, several seismic attributes are analyzed in this section: the local structural dip, chaos, RMS amplitude, and variance. The local structural dip is used to better identify and specify the location and distribution of signal distortion beneath the channel anomalies⁵². Chaos and variance attributes also highlight the incoherency proximal to the channel anomalies.

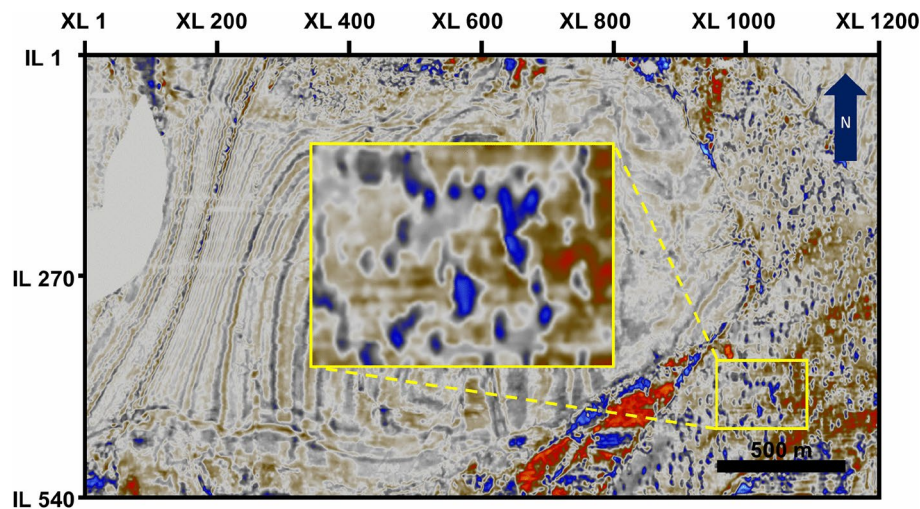


Figure 10. Timeslice at 71 ms; Illustration of “polka-dot” anomaly. The yellow box marks a magnified view of polka-dot anomalies. This figure was generated using the Petrel software (<https://www.software.slb.com/products/petrel>).

However, in this study, they are also used to characterize shallow geological features such as faults⁶⁹. RMS amplitude in this study emphasizes the impedance contrast in the formation that contains the seismic anomalies and possible lithology changes⁴⁷. Figure 11 shows the results of the seismic attribute analysis for inline section 145.

Figure 11a shows the original seismic data. Distinctive amplitude contrasts with pockmarks on top and signal distortion beneath the anomalies are observed. Figure 11b is an attribute analysis of a local structural dip. It is clear that the previously observed signal-hindered region in the original seismic section has a higher local dip variance than the neighboring region. This type of signal distortion is known as acoustic blanking and is often observed in shallow gas deposits because fluid/gas-saturated pore spaces absorb the energy of propagated seismic waves^{70,71}.

Figure 11c is a chaos attribute of the original data. High chaos values are observed in the signal-hindered region⁵². Again, the hindering of signals beneath the anomalies is clearly visible. In addition to the region beneath the anomaly, two slanted lineations parallel to each other are observed and marked by a bright purple box. These lineations seem to represent the shallow reverse faults that formed relatively recently. These faults are better illustrated in Fig. 12. Figure 12 is a timeslice of a variance attribute analysis result at 53 ms. A variance attribute is used to emphasize the discontinuity in the seismic volume and to easily identify the faults⁵². The strike of these faults is NNE-SSW which is aligned with the strike of F1 (Fig. 5). This may imply that the tectonic regime that formed F1 also formed these shallow faults, indicating that this tectonic regime is currently active or has been active until recently⁷².

Figure 11d shows the RMS amplitude of the original seismic data. As expected, the amplitude contrast is well emphasized by the high RMS amplitude values. High RMS values may indicate high-porosity lithologies such as porous sandstone^{43,47,73,74}. Based on these observations, it can be concluded that the structural and signal behaviors of channel anomalies are in accordance with the typical characteristics of gas deposits where acoustic blanking, pockmarks, and amplitude contrast between fluid-saturated-low-acoustic impedance zone and high-acoustic impedance zone exists⁴⁷.

Another important observation can be made by analyzing the variance attribute of the channel anomaly. As mentioned previously, channel anomalies exhibit channel-like features when viewed in a timeslice (Fig. 9). Previously observed channel-like features show a clear dendritic pattern branching into the structural high region of the volume (Fig. 13). This sedimentary pattern resembles a tidal channel formed in a gently dipping shoreface environment⁷⁵. Further discussion on these incisions is provided in a later section.

Due to the abnormal behavior of polka-dot anomalies, several candidates potentially responsible for the polka-dot anomalies have been examined based on their shapes and characteristics: pinnacle reefs, dolines, and concretions. Pinnacle reefs are carbonate structures that form during rapid sea level rise. In time/depth slices, they exhibit a circular polka-dot-like geometry^{60,61}. However, this candidate was eliminated since there is no evidence of carbonate deposits on the eastern Korean Peninsula and since the acoustic impedance does not match that of the polka-dot anomaly. Additionally, the diameter of pinnacle reefs often reaches a few hundred meters, which is much greater than the size range of the polka-dot anomaly in this study.

Another candidate is dolines, which are found in karst environments. Dolines result from the subsidence and collapse of karst areas^{62,63}, which results in the formation of circular crater-like features⁷⁶. The size of the dolines ranges up to a few tens of meters, which is similar to the size of the polka-dot anomaly. However, there is no sedimentary evidence on the eastern continental margin of the Korean Peninsula indicating karst formation; hence, this candidate was also eliminated.

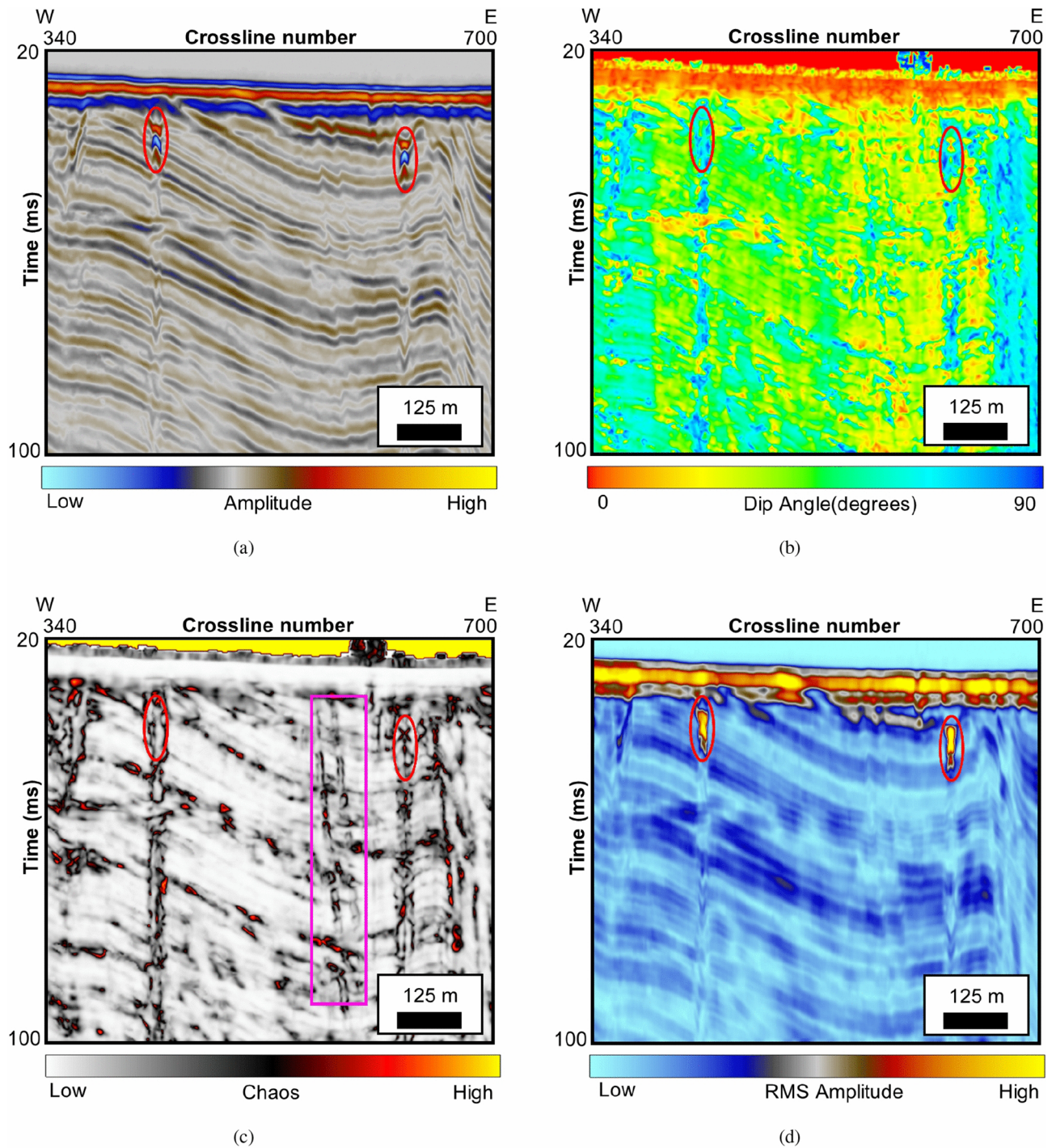


Figure 11. Seismic attribute analysis of channel anomalies (marked by red circle) in inline 145: (a) original seismic, (b) local structural dip, (c) chaos with shallow faults marked by bright purple box, (d) RMS amplitude. Note that the section was cropped to better visualize the channel anomalies. Notice the signal hindered region beneath the channel anomalies are consistent throughout the attribute analysis. The figure is vertically exaggerated by the factor of 8.4. Refer to Fig. 6 for location. This figure was generated using the Petrel software (<https://www.software.slb.com/products/petrel>).

The final candidate is a concretion that results from mineral precipitation within an unconsolidated formation^{64,65}. This candidate was eliminated since the sizes of the concretions (a few centimeters to a few meters) do not match the dimensions of the polka-dot anomalies. Furthermore, the phase behavior observed in the data indicates that the acoustic impedance of the polka-dot anomalies is lower than that of the surrounding material, which would not be true if they were concretions since precipitated minerals almost always result in greater acoustic impedance than the surrounding material.

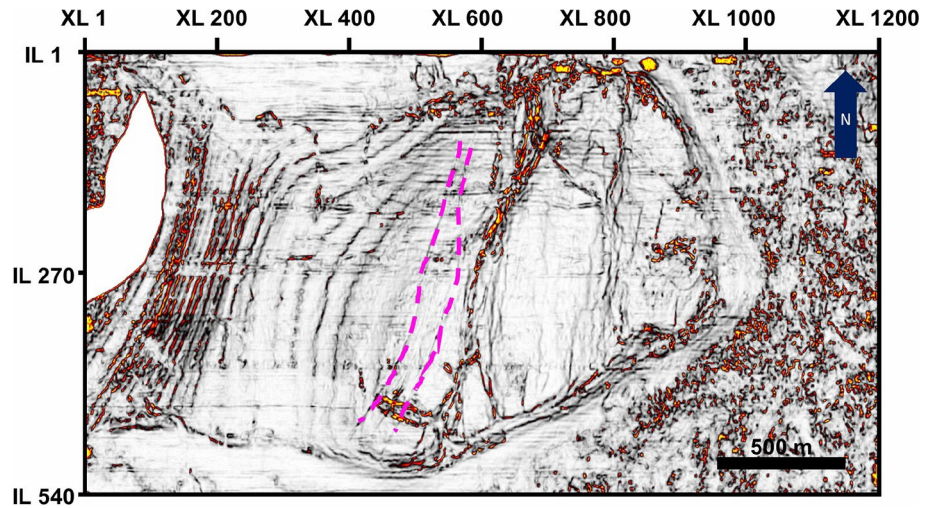


Figure 12. Timeslice at 53 ms of variance attribute illustrating shallow faults (dashed-bright purple lines) found in Fig. 11c. Note that the strike of these faults is aligned with the strike of F1 shown in Fig. 5. This figure was generated using the Petrel software (<https://www.software.slb.com/products/petrel>).

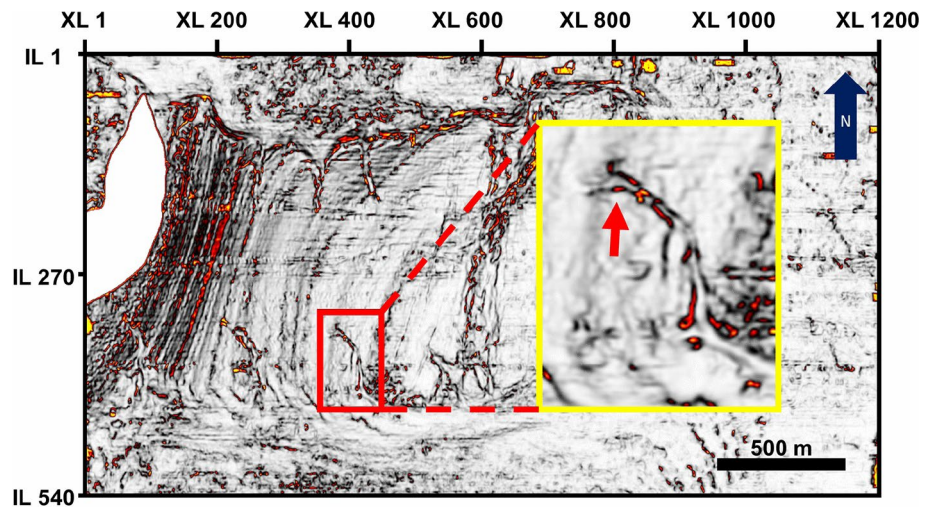


Figure 13. Timeslice at 39 ms in variance attribute. Clear channels with dendritic pattern (marked by red arrow) branching into the structural high region are visible. The yellow box shows magnified view of a channel. This figure was generated using the Petrel software (<https://www.software.slb.com/products/petrel>).

After eliminating the abovementioned candidates, it is concluded that shallow gas deposits are the most likely and realistic candidates. Hence, the seismic attributes often used to identify gas deposits are used to analyze the polka-dot anomalies. RMS amplitude, sweetness, and envelope are chosen for attribute analysis. Sweetness is used to identify “sweet spots” where oil and gas are prone by analyzing the amplitude and frequency component of the formation^{49,77}. The envelope is chosen to identify the zone of acoustic impedance change which potentially indicates the hydrocarbon accumulation^{43,44,47}. The results of the seismic attribute analysis of the polka-dot anomaly are shown in Fig. 14. Figure 14a shows the original seismic data. Few bright spots are evident, and pillar-like structures within these bright spots are also shown. Figure 14b is an RMS amplitude attribute analysis result emphasizing the bright spots with high RMS amplitudes. Figure 14c is a sweetness attribute analysis result that indicates that bright spots are possible regions of sandy formation that can act as reservoirs. High sweetness values characterize high-amplitude and low-frequency regions such as sandy reservoirs. In contrast, low sweetness values characterize low-amplitude and high-frequency regions, indicating a possible shale reservoir^{49,77}. Here, high sweetness values are well aligned with the bright spots initially observed in the original seismic section (Fig. 14a). Figure 14d shows an envelope attribute analysis result of the seismic data that highlights the high-envelope-amplitude region. The sharp change in the envelope of the purple circles may be an indicator of lithology change⁴⁴. Based on the seismic attribute analysis, similar to channel anomalies, the polka-dot anomalies are most likely shallow gas deposits.

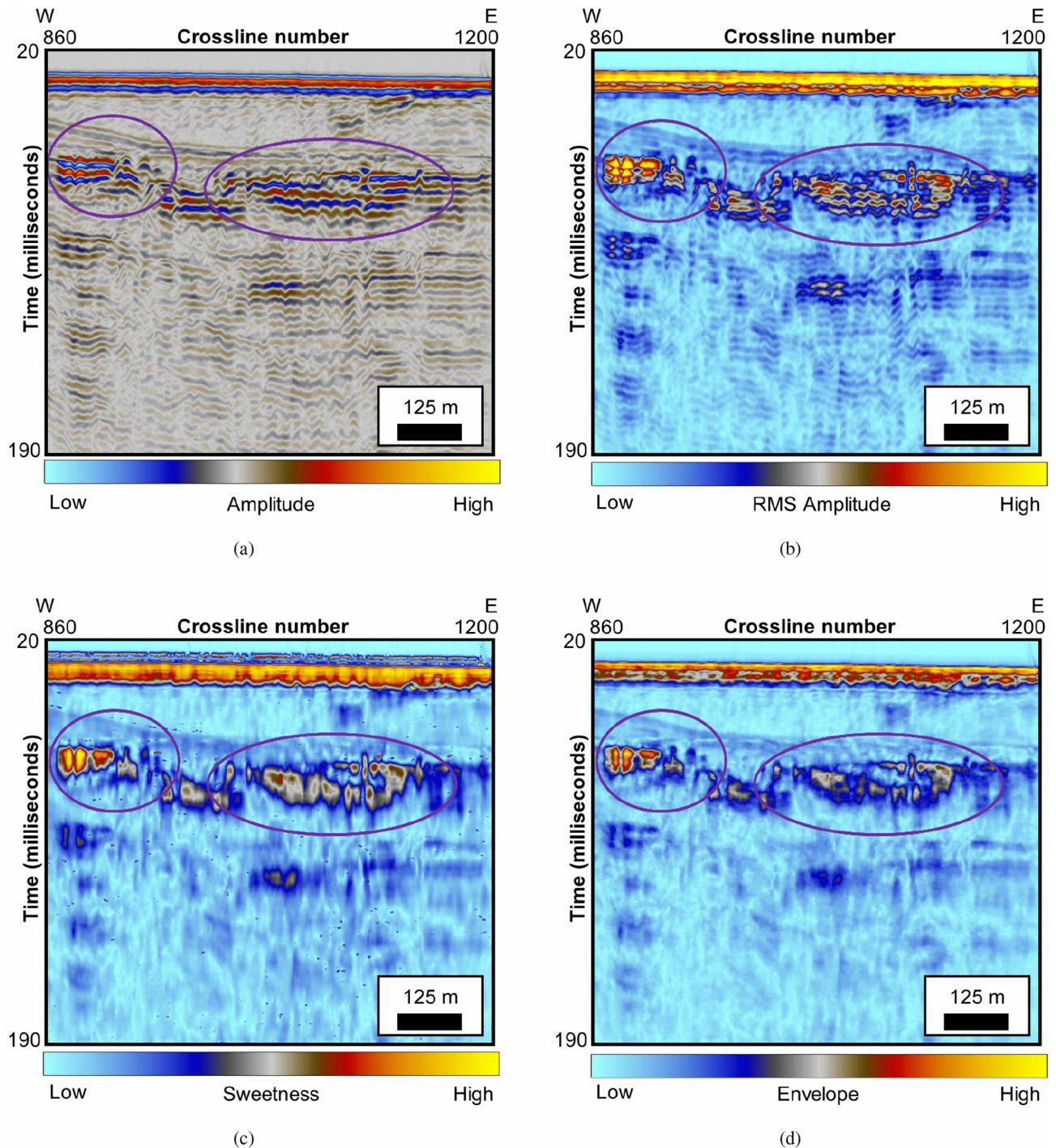


Figure 14. Seismic attribute analysis of polka-dot anomaly (marked by purple circles) in inline 378: (a) original seismic, (b) rms amplitude, (c) sweetness, (d) envelope. Note that the section was cropped to visualize the polka-dot anomalies better. The figure is vertically exaggerated by the factor of 3.7. Refer to Fig. 6 for location. This figure was generated using the Petrel software (<https://www.software.slb.com/products/petrel>).

Geological scenario reconstruction

There still exists uncertainty regarding the absolute temporal information on the stratigraphy due to the lack of drilling data within the seismic volume of the study. To mitigate this problem, the horizons interpreted in this study were traced from the drilling data and seismic data from regions proximal to the study area located within Yeongil Bay and Pohang Basin based on the depositional patterns and the seismic facies analysis. Preceding researches on the stratigraphy of Yeongil Bay and the East Sea are also taken into account in determining the stratigraphic boundaries in the data used in this study^{54,78}.

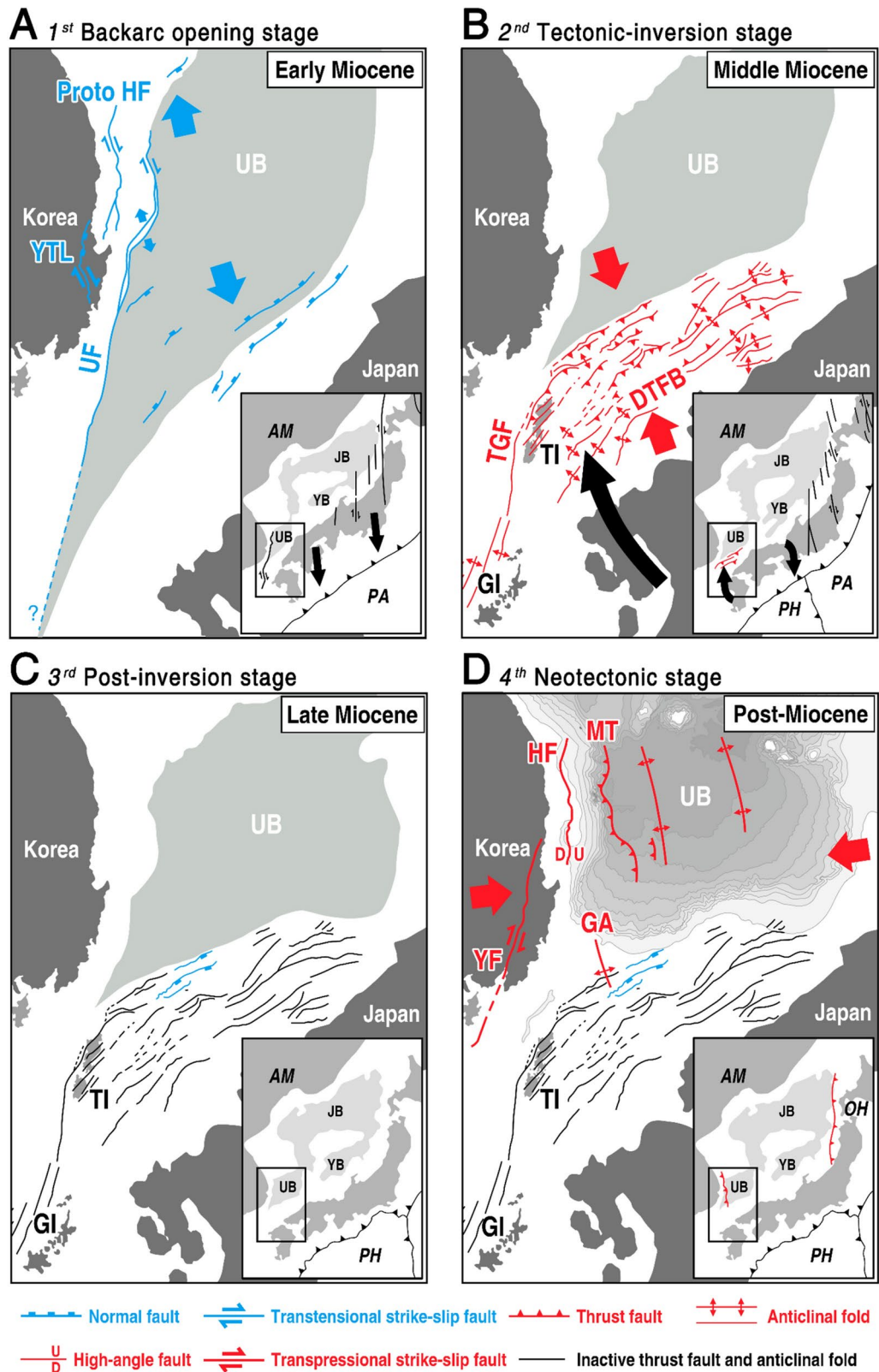


Figure 15. Four-stage tectonic model of the East Sea (modified after¹⁶): (a) back-arc opening stage (Early Miocene), (b) Tectonic-inversion stage (Middle Miocene), (c) Post-inversion stage (Late Miocene), and (d) Neotectonic stage (Post-Miocene to present). AM: Amur Plate, PA: Pacific Plate, PH: Philippine Sea Plate, OH: Okhotsk Plate, UB: Ulleung Basin, YB: Yamato Basin, JB: Japan Basin, TI: Tsushima Island, GI: Goto Island, YTL: Yeonil Tectonic Line, UF: Ulleung Fault. TGF: Tsushima-Goto Fault, DTFB: Dolgorae Thrust-Fold Belt, YF: Yangsan Fault, HF: Hupo Fault, MT: Major Thrust, GA: Gorae Anticline.

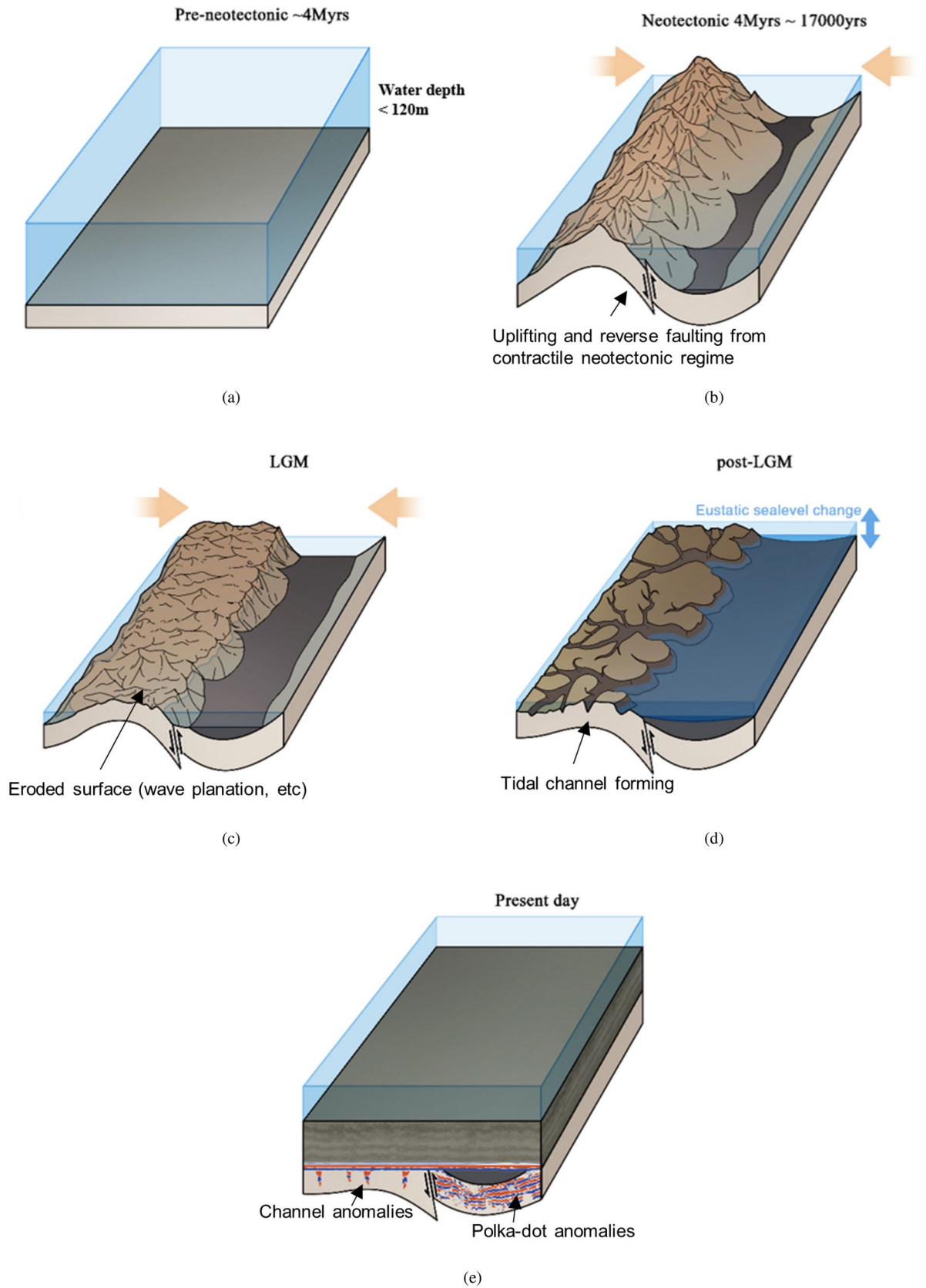


Figure 16. Illustration of anomalies formation: (a) Pre-neotectonic to 4Ma, (b) 4Ma to 17,000 yrs, (c) Last Glacial Maximum, (d) Post-LGM, and (e) Present day. This figure was generated using the Adobe Illustrator software (<https://www.adobe.com/products/illustrator.html>).

A geological reconstruction of anomaly formation is provided in this section. To develop an insight into the deformation process following the formation of the back-arc basin (the East Sea, in this case), it is crucial to integrate the observation of anomalies with the broader context of a geological process of the region. To interpret the geology of the seismic anomalies, it is necessary to revisit the tectonic implications of the eastern continental margin of the Korean Peninsula. Until very recently, the back-arc opening of the East Sea was thought to be divided into three major stages as mentioned in the introduction. This was mainly due to the lack of data of good quality and detailed analysis. However, the seismic anomalies in this study are located in the shallow, near-surface region of the seismic volume (Figs. 7 and 8), and therefore cannot be explained by contractional deformation in the late middle Miocene. From the multiattribute analysis performed in the previous section, we have identified the physical characteristics of the seismic anomalies. In this section, the formation of channel and polka-dot anomalies are investigated with respect to the context of the post-rifting contractional deformation of the East Sea.

To reconstruct the formation process behind the anomalies, this study focuses on the major characteristics of the anomalies. Both anomalies are located in relatively shallow deposits compared to the F1 which is most likely formed during the late Miocene tectonic inversion^{2,34}. This indicates the anomalies have been formed due to the geological process that took place in the post-Miocene era. Considering that channel anomalies are constrained in the uplifted region of the study area and the channel anomalies resemble that of the tidal channel, we suggest that the post-Miocene contractional force must have been present so that the formation could be uplifted and exposed to the tidal environment. The overburden of the polka-dot anomalies can also be explained by this phenomenon since the overburden consists of post-neotectonic deposits. Based on the fact that the channel anomalies are dendritic into the structural high and considering the current sea level of the region, we can also propose that the region had undergone a sea level drop after the uplifting. Detailed descriptions of these geological processes are provided in the following sections.

This study proposes two major geological events that are thought to be the main causes of the formation of the anomalies: post-Miocene neotectonics and the Last Glacial Maximum. At approximately 4 Ma, the Amur Plate began to move eastward relative to the Pacific Plate¹⁵. This plate motion led to a compressional stress regime, referred to as neotectonics, in northeastern Asia, deforming the East Sea^{16,79}. Figure 15 illustrates a four-stage tectonic model of the East Sea from the beginning of the back-arc opening to the post-Miocene neotectonic stage suggested by¹⁶. During the post-Miocene neotectonic stage, the southeastern region of the Korean Peninsula experienced a regional E-W compressional stress field. This stress field resulted in an uplift in the Yeongil Bay and subsequently formed the structural high and topographic low. The compressional stress field also formed a fold and high-angle reverse fault (F1), as shown in Fig. 4. Furthermore, the shallow faults in Fig. 12 are also thought to have formed during the neotectonic stage considering that the shallow faults share a similar strike direction with F1 (Figs. 6 and 12).

Another event that played a crucial role in anomaly formation was the Last Glacial Maximum (LGM), which occurred in the late Pleistocene⁸⁰. During this time, the global sea level was estimated to have decreased by approximately 120 m⁸¹. Based on the current bathymetry of the East Sea, the region of study must have been subaerially exposed above sea level at the time. Combined with the neotectonics that uplifted the region, during this time, the uplifted region underwent erosion and wave planation, which resulted in an unconformable interface (H3). Subsequently, following the LGM, uplifted and eroded pre-neotectonic formations experienced a tide-dominated environment during the phase of eustatic sea level change during which tidal channels formed, as shown in Fig. 13. Later, these incisions were filled by post-neotectonic sediment and subsequently saturated with shallow gas. Post-neotectonic sediment was also deposited in the topographic low. These deposits overlie the top of the polka-dot anomaly. The processes of channel and polka-dot anomaly formation are illustrated in Fig. 16.

The major difference between the channel anomalies and the polka-dot anomalies is that the channel anomalies are overlain by pockmarks. A pockmark is formed during gas or fluid leakage and subsidence of the overlying bedding⁸². This feature is not found in the polka-dot anomalies. This can be attributed to the difference in overburden on each anomaly. A channel anomaly is located within the structural high region, which has been uplifted by neotectonics and consequently eroded. These processes led to a decrease in the overburden pressure and hence the easier leakage of shallow gas, leading to the formation of pockmarks. In contrast, the polka-dot anomalies are located in the region of the topographic low. This region has thicker sediments than the region containing a channel anomaly. The heavier overburden pressure suppressed the escape of shallow gas from the reservoir, but without complete sealing, some of the gas leaked into the overlying formation, forming the polka-dot anomalies.

Conclusion

3D shallow water seismic data was acquired by the EOS streamer system in Yeongil Bay, Pohang. Conventional marine seismic data processing sequence was applied and brief seismic interpretation revealed that the data contains two major seismic anomalies, channel and polka-dot anomalies, named after their appearances. This study provides an insight into a process of contractional deformation in back-arc basin via two major steps: a multiattribute analysis of seismic anomalies and geological reconstruction of anomalies formation.

A multiattribute analysis was performed from both geophysical and geological perspectives to further characterize the physical behavior of the anomalies. As for channel anomalies, local dip angle and chaos attributes revealed the signal-hindered region beneath the channel anomalies indicating a possible fluid saturation in the channel anomalies. A chaos attribute analysis revealed a pair of shallow faults which are used to constrain the temporal information of contractional deformation that the region has undergone. A porous lithology was highlighted by the RMS amplitude analysis. From these observations, the channel anomalies in the data were identified as shallow gas deposits. For polka-dot anomalies, several candidates were proposed based on the

physical geometry and shape. However, after multiattribute analysis utilizing RMS amplitude, sweetness, and envelope, the polka-dot anomalies present in the data were concluded most likely to be shallow gas deposits.

This paper attributes the formation of these anomalies to two major geological events in the post-Miocene to Pleistocene age in the evolution of the southeastern Korean Peninsula. The post-Miocene neotectonic contractional deformation resulted in the uplifting in the region of study. Subsequently, the LGM led to the erosion and excavation into the structural high of the region leading to the formation of tidal channels. Following the LGM, the overburden was deposited on top of the channel and polka-dot anomalies. The difference in thickness of overburden has led to the different rates of gas leakage in these anomalies. From these processes, this paper provides an insight into the geology of the continental margin of the southeastern Korean Peninsula where a geological interpretation of Quaternary structures has not been actively studied yet.

Data availability

The data that support the findings of this study are available from the Korea Institute of Geoscience and Mineral Resources (KIGAM) but restrictions apply to the availability of these data, which were used under license for the current study, and so are not publicly available. Data are however available upon reasonable request to J. Ha (jihoha@kigam.re.kr) and with permission of KIGAM.

Received: 29 February 2024; Accepted: 1 October 2024

Published online: 16 October 2024

References

1. Tamaki, K. Geological structure of the Japan sea and its tectonic implications. *Chishitsu Chosasho Geppo(Japan)* **39** (1988).
2. Yoon, S. H. & Chough, S. K. Regional strike slip in the eastern continental margin of Korea and its tectonic implications for the evolution of ulleung basin, east sea (sea of Japan). *Geol. Soc. Am. Bull.* **107**, 83 (1995).
3. Chough, S. K. & Barg, E. Tectonic history of ulleung basin margin, east sea (sea of Japan). *Geology* **15**, 45 (1987).
4. Kim, H.-J., Han, S.-J., Lee, G. H. & Huh, S. Seismic study of the ulleung basin crust and its implications for the opening of the east sea (Japan sea). *Mar. Geophys. Res.* **20**, 219–237. <https://doi.org/10.1023/a:1004573816915> (1998).
5. Lee, Y. S., Ishikawa, N. & Kim, W. K. Paleomagnetism of tertiary rocks on the Korean peninsula: Tectonic implications for the opening of the east sea (sea of Japan). *Tectonophysics* **304**, 131–149. [https://doi.org/10.1016/s0040-1951\(98\)00270-4](https://doi.org/10.1016/s0040-1951(98)00270-4) (1999).
6. Kim, Y.-J. et al. Identification of shallow gas by seismic data and avo processing: Example from the southwestern continental shelf of the Ulleung basin, east sea, Korea. *Mar. Pet. Geol.* **117**, 104346. <https://doi.org/10.1016/j.marpetgeo.2020.104346> (2020).
7. Horozal, S. et al. Seismic evidence of shallow gas in sediments on the southeastern continental shelf of Korea, east sea (Japan sea). *Mar. Pet. Geol.* **133**, 105291. <https://doi.org/10.1016/j.marpetgeo.2021.105291> (2021).
8. Lee, S. H. & Chough, S. K. Distribution and origin of shallow gas in deep-sea sediments of the Ulleung basin, east sea (sea of Japan). *Geo-Mar. Lett.* **22**, 204–209. <https://doi.org/10.1007/s00367-002-0114-x> (2002).
9. Otofujii, Y. & Matsuda, T. Paleomagnetic evidence for the clockwise rotation of southwest Japan. *Earth Planet. Sci. Lett.* **62**, 349–359. [https://doi.org/10.1016/0012-821x\(83\)90005-5](https://doi.org/10.1016/0012-821x(83)90005-5) (1983).
10. Otofujii, Y.-I., Matsuda, T. & Nohda, S. Paleomagnetic evidence for the miocene counter-clockwise rotation of northeast Japan-rifting process of the Japan arc. *Earth Planet. Sci. Lett.* **75**, 265–277. [https://doi.org/10.1016/0012-821x\(85\)90108-6](https://doi.org/10.1016/0012-821x(85)90108-6) (1985).
11. Celaya, M. & McCabe, R. Kinematic model for the opening of the sea of Japan and the bending of the Japanese islands. *Geology* **15**, 53 (1987).
12. Faure, M. & Lalevée, F. Bent structural trends of Japan: Flexural-slip folding related to the neogene opening of the sea of Japan. *Geology* **15**, 49 (1987).
13. Lallemand, S. & Jolivet, L. Japan sea: A pull-apart basin?. *Earth Planet. Sci. Lett.* **76**, 375–389. [https://doi.org/10.1016/0012-821x\(86\)90088-9](https://doi.org/10.1016/0012-821x(86)90088-9) (1986).
14. Kimura, G. & Tamaki, K. Collision, rotation, and back-arc spreading in the region of the Okhotsk and Japan seas. *Tectonics* **5**, 389–401. <https://doi.org/10.1029/tc005i003p00389> (1986).
15. Taira, A. Tectonic evolution of the Japanese island arc system. *Annu. Rev. Earth Planet. Sci.* **29**, 109–134. <https://doi.org/10.1146/annurev.earth.29.1.109> (2001).
16. Lee, J.-H. et al. Two distinct back-arc closure phases of the east sea: Stratigraphic evidence from the sw ulleung basin margin. *Front. Earth Sci.* [SPACE] <https://doi.org/10.3389/feart.2022.839712> (2022).
17. Ingle, J. J. Subsidence of the Japan Sea: Stratigraphic Evidence from odp Sites and Onshore Sections. In *Proceedings of the Ocean Drilling Program* [SPACE] <https://doi.org/10.2973/odp.proc.sr.127128-2.132.1992> (1992) (**Ocean Drilling Program**).
18. Jolivet, L. & Tamaki, K. Neogene Kinematics in the Japan Sea Region and Volcanic Activity of the Northeast Japan arc. In *Proceedings of the Ocean Drilling Program* [SPACE] <https://doi.org/10.2973/odp.proc.sr.127128-2.239.1992> (1992) (**Ocean Drilling Program**).
19. Lee, G. H. et al. Structural evolution of the southwestern margin of the ulleung basin, east sea (Japan sea) and tectonic implications. *Tectonophysics* **502**, 293–307. <https://doi.org/10.1016/j.tecto.2011.01.015> (2011).
20. Kim, G. B. & Yoon, S.-H. An insight into asymmetric back-arc extension: Tecto-magmatic evidences from the ulleung basin, the east sea (sea of Japan). *Tectonophysics* **717**, 182–192. <https://doi.org/10.1016/j.tecto.2017.07.016> (2017).
21. Shin, J., Ha, J., Kang, N.-K., Kim, H.-D. & Kim, C.-S. Development of a portable 3d seismic survey system for nearshore surveys and the first case study offshore Pohang, South Korea. *Marine Geophys. Res.* [SPACE] <https://doi.org/10.1007/s11001-021-09453-x> (2021).
22. Ryang, W. H., Simms, A. R., Yoon, H. H., Chun, S. S. & Kong, G. S. Last interglacial sea-level proxies in the Korean peninsula. *Earth Syst. Sci. Data* **14**, 117–142. <https://doi.org/10.5194/essd-14-117-2022> (2022).
23. Løseth, H., Gading, M. & Wensaas, L. Hydrocarbon leakage interpreted on seismic data. *Mar. Pet. Geol.* **26**, 1304–1319. <https://doi.org/10.1016/j.marpetgeo.2008.09.008> (2009).
24. Davis, A. Shallow gas: An overview. *Cont. Shelf Res.* **12**, 1077–1079. [https://doi.org/10.1016/0278-4343\(92\)90069-v](https://doi.org/10.1016/0278-4343(92)90069-v) (1992).
25. Clarke, R. *Seabed Pockmarks and Seepages—Impact on Geology, Biology and the Marine Environment*, vol. 6 (Elsevier BV, 1989).
26. Schroot, B. North Sea Shallow Gas as a Natural Analogue in Feasibility Studies on CO₂ Sequestration. In *64th EAGE Conference and Exhibition*, <https://doi.org/10.3997/2214-4609-pdb.5.h010> (European Association of Geoscientists and Engineers, 2002).
27. Judd, A. & Hovland, M. The evidence of shallow gas in marine sediments. *Cont. Shelf Res.* **12**, 1081–1095. [https://doi.org/10.1016/0278-4343\(92\)90070-z](https://doi.org/10.1016/0278-4343(92)90070-z) (1992).
28. Ryu, B.-J. et al. Gas hydrates in the western deep-water ulleung basin, east sea of Korea. *Mar. Pet. Geol.* **26**, 1483–1498. <https://doi.org/10.1016/j.marpetgeo.2009.02.004> (2009).
29. Lee, D., Kim, B.-Y., Kim, J.-S. & Jang, S. Shallow gas exploration in the Pohang basin transition zone. *Geophys. Geophys. Explor.* **25**, 1–13. <https://doi.org/10.7582/GGE.2022.25.1.1> (2022).

30. Lee, D.-H. et al. Geochemical signatures of organic matter associated with gas generation in the Pohang basin, south Korea. *Geosci. J.* **26**, 555–567. <https://doi.org/10.1007/s12303-021-0046-y> (2022).
31. Yoon, S., Sohn, Y. & Chough, S. Tectonic, sedimentary, and volcanic evolution of a back-arc basin in the east sea (sea of Japan). *Mar. Geol.* **352**, 70–88. <https://doi.org/10.1016/j.margeo.2014.03.004> (2014).
32. Choe, M. Y. & Chough, S. K. The hunghae formation, se korea: Miocene debris aprons in a back-arc intraslope basin. *Sedimentology* **35**, 239–255. <https://doi.org/10.1111/j.1365-3091.1988.tb00947.x> (1988).
33. Chough, S. K., Choe, M. Y. & Hwang, I. G. The miocene dousman fan-delta, southeast Korea: A composite fan-delta system in back-arc margin. *SEPM J. Sediment. Res.* [SPACE] <https://doi.org/10.1306/212f91ba-2b24-11d7-8648000102c1865d> (1990).
34. Yoon, S., Chang, K.-H., You, H.-S. & Lee, Y.-G. Tectonic history of the tertiary basins of the southern Korean peninsula. *Econ. Environ. Geol.* **24**, 301–308 (1991).
35. Dondurur, D. *Acquisition and Processing of Marine Seismic Data* (2018).
36. Larner, K., Chambers, R., Yang, M., Lynn, W. & Wai, W. Coherent noise in marine seismic data. *Geophysics* **48**, 854–886. <https://doi.org/10.1190/1.1441516> (1983).
37. Yilmaz, Ö. *Seismic Data Analysis: Processing, Inversion, and Interpretation of Seismic Data* (Society of Exploration Geophysicists, 2001).
38. Lee, H.-Y. et al. Resolution analysis of shallow marine seismic data acquired using an airgun and an 8-channel streamer cable. *J. Appl. Geophys.* **105**, 203–212. <https://doi.org/10.1016/j.jappgeo.2014.03.021> (2014).
39. Wardell, N., Diviaco, P. & Sinceri, R. 3d pre-processing techniques for marine vhr seismic data. *First break* [SPACE] <https://doi.org/10.1046/j.1365-2397.2002.00291.x> (2002).
40. Lee, H.-Y. et al. High-resolution shallow marine seismic surveys off busan and pohang, Korea, using a small-scale multichannel system. *J. Appl. Geophys.* **56**, 1–15. <https://doi.org/10.1016/j.jappgeo.2004.03.003> (2004).
41. Stolt, R. H. Migration by Fourier transform. *GEOPHYSICS* **43**, 23–48. <https://doi.org/10.1190/1.1440826> (1978).
42. Morley, L. & Claerbout, J. Predictive deconvolution in shot-receiver space. *GEOPHYSICS* **48**, 515–531. <https://doi.org/10.1190/1.1441483> (1983).
43. Barnes, A. E. *Handbook of Poststack Seismic Attributes* (Society of Exploration Geophysicists, 2016).
44. Chopra, S. & Marfurt, K. J. Seismic attributes—a historical perspective. *Geophysics* **70**, 30–280. <https://doi.org/10.1190/1.2098670> (2005).
45. Chen, Q. & Sidney, S. Seismic attribute technology for reservoir forecasting and monitoring. *Lead. Edge* **16**, 445–448. <https://doi.org/10.1190/1.1437657> (1997).
46. Kenney, J. F. & Keeping, E. Root mean square. *Math. Stat.* **1**, 59–60 (1962).
47. Brown, A. R. *Interpretation of Three-Dimensional Seismic Data* (American Association of Petroleum Geologists, 2011).
48. Taner, M. T., Schuelke, J. S., O'Doherty, R. & Baysal, E. *Seismic Attributes Revisited*, 1104–1106 (2005).
49. Radovich, B. J. & Oliveros, R. B. 3-d sequence interpretation of seismic instantaneous attributes from the gorgon field. *Lead. Edge* **17**, 1286–1293. <https://doi.org/10.1190/1.1438125> (1998).
50. Chopra, S. & Marfurt, K. J. *Seismic Attributes for Prospect Identification and Reservoir Characterization* (Society of Exploration Geophysicists and European Association of Geoscientists and Engineers, 2007).
51. Tingdahl, K. M. & de Groot, P. F. Post-stack dip-and azimuth processing. *J. Seism. Explor.* **12**, 113–126 (2003).
52. Koson, S., Chenrai, P. & Choowong, M. Seismic attributes and their applications in seismic geomorphology. *Bull. Earth Sci. Thailand* **6**, 1–9 (2013).
53. Pigott, J. D., Kang, M.-H. & Han, H.-C. First order seismic attributes for clastic seismic facies interpretation: Examples from the east china sea. *J. Asian Earth Sci.* **66**, 34–54. <https://doi.org/10.1016/j.jseae.2012.11.043> (2013).
54. Sohn, Y., Rhee, C. & Shon, H. Revised stratigraphy and reinterpretation of the miocene pohang basinfill, se Korea: Sequence development in response to tectonism and eustasy in a back-arc basin margin. *Sed. Geol.* **143**, 265–285. [https://doi.org/10.1016/S0037-0738\(01\)00100-2](https://doi.org/10.1016/S0037-0738(01)00100-2) (2001).
55. Marfurt, K. J. & Alves, T. M. Pitfalls and limitations in seismic attribute interpretation of tectonic features. *Interpretation* **3**, SB5–SB15. <https://doi.org/10.1190/int-2014-0122.1> (2015).
56. Bachrach, R. & Nur, A. High-resolution shallow-seismic experiments in sand, part i: Water table, fluid flow, and saturation. *Geophysics* **63**, 1225–1233. <https://doi.org/10.1190/1.1444423> (1998).
57. Nanda, N. C. *Seismic Reflection Principles: Basics*, 19–35 (Springer International Publishing, 2016).
58. Lericolais, G., Auffret, J. & Bourillet, J. The quaternary channel river: Seismic stratigraphy of its palaeo-valleys and deeps. *J. Quat. Sci.* **18**, 245–260. <https://doi.org/10.1002/jqs.759> (2003).
59. Gee, M., Gawthorpe, R., Bakke, K. & Friedmann, S. Seismic geomorphology and evolution of submarine channels from the angolan continental margin. *J. Sediment. Res.* **77**, 433–446. <https://doi.org/10.2110/jsr.2007.042> (2007).
60. Grahame, J. & Cole, V. Prospectivity of the triassic successions of the north west shelf of Australia: New insights from a regional integrated geoscience study. *Lead. Edge* **40**, 172–177. <https://doi.org/10.1190/le40030172.1> (2021).
61. McLaughlin, P. I. et al. The rise of pinnacle reefs: A step change in marine evolution triggered by perturbation of the global carbon cycle. *Earth Planet. Sci. Lett.* **515**, 13–25. <https://doi.org/10.1016/j.epsl.2019.02.039> (2019).
62. Mihevc, A. & Mihevc, R. Morphological characteristics and distribution of dolines in Slovenia, a study of a lidar-based doline map of Slovenia. *Acta Carsologica* [SPACE] <https://doi.org/10.3986/ac.v50i1.9462> (2021).
63. Sauro, U. *Closed Depressions in Karst Areas*, 140–155 (2012).
64. Marshall, J. D. & Pirrie, D. Carbonate concretions—explained. *Geol. Today* **29**, 53–62. <https://doi.org/10.1111/gto.12002> (2013).
65. Collinson, J. Sedimentary processes | post-depositional sedimentary structures. In *Encyclopedia of Geology*, 602–611. <https://doi.org/10.1016/b0-12-369396-9/00467-6> (Elsevier, 2005).
66. Cukur, D., Krastel, S., Tomonaga, Y., Çağatay, M. N. & Meydan, A. F. Seismic evidence of shallow gas from lake van, eastern Turkey. *Mar. Pet. Geol.* **48**, 341–353. <https://doi.org/10.1016/j.marpetgeo.2013.08.017> (2013).
67. White, R. S. Seismic bright spots in the gulf of Oman. *Earth Planet. Sci. Lett.* **37**, 29–37. [https://doi.org/10.1016/0012-821x\(77\)90143-1](https://doi.org/10.1016/0012-821x(77)90143-1) (1977).
68. Hustoft, S., Bünz, S. & Mienert, J. Three-dimensional seismic analysis of the morphology and spatial distribution of chimneys beneath the nyegga pockmark field, offshore mid-Norway. *Basin Res.* **22**, 465–480. <https://doi.org/10.1111/j.1365-2117.2010.00486.x> (2010).
69. Silva, C. C., Marcolino, C. S. & Lima, F. D. Automatic fault extraction using ant tracking algorithm in the marlim south field, campos basin. In *SEG Technical Program Expanded Abstracts 2005*, <https://doi.org/10.1190/1.2148294> (Society of Exploration Geophysicists, 2005).
70. Schroot, B. M. & Schüttenhelm, R. T. Shallow gas and gas seepage: expressions on seismic and other acoustic data from the netherlands north sea. *J. Geochem. Explor.* **78–79**, 305–309. [https://doi.org/10.1016/S0375-6742\(03\)00112-2](https://doi.org/10.1016/S0375-6742(03)00112-2) (2003).
71. Missiaen, T., Murphy, S., Loncke, L. & Henriët, J.-P. Very high-resolution seismic mapping of shallow gas in the belgian coastal zone. *Cont. Shelf Res.* **22**, 2291–2301. [https://doi.org/10.1016/S0278-4343\(02\)00056-0](https://doi.org/10.1016/S0278-4343(02)00056-0) (2002).
72. Nieto-Samaniego, A. & Alaniz-Alvarez, S. Origin and tectonic interpretation of multiple fault patterns. *Tectonophysics* **270**, 197–206. [https://doi.org/10.1016/S0040-1951\(96\)00216-8](https://doi.org/10.1016/S0040-1951(96)00216-8) (1997).
73. Omoja, U. C. & Obiekezie, T. N. Application of 3d seismic attribute analyses for hydrocarbon prospectivity in uzot-field, onshore niger delta basin, nigeria. *Int. J. Geophys.* **1–11**, 2019. <https://doi.org/10.1155/2019/1706416> (2019).

74. Emujakporue, G. O. & Enyenihi, E. E. Identification of seismic attributes for hydrocarbon prospecting of akos field, niger delta, Nigeria. *SN Appl. Sci.* [SPACE] <https://doi.org/10.1007/s42452-020-2570-1> (2020).
75. ZhenXia, L. et al. Tidal deposition systems of china's continental shelf, with special reference to the eastern bohai sea. *Mar. Geol.* **145**, 225–253. [https://doi.org/10.1016/s0025-3227\(97\)00116-3](https://doi.org/10.1016/s0025-3227(97)00116-3) (1998).
76. Fournillon, A. et al. *Characterization of a Paleokarstic Oil Field (Rospo Mare, Italy): Sedimentologic and Diagenetic Outcomes, and Their Integration in Reservoir Simulation*, 47–55 (Springer International Publishing, 2017).
77. Hart, B. S. Channel detection in 3-d seismic data using sweetness. *AAPG Bull.* **92**, 733–742. <https://doi.org/10.1306/02050807127> (2008).
78. Hwang, I., Chough, S., Hong, S. & Choe, M. Controls and evolution of fan delta systems in the miocene pohang basin, se Korea. *Sed. Geol.* **98**, 147–179. [https://doi.org/10.1016/0037-0738\(95\)00031-3](https://doi.org/10.1016/0037-0738(95)00031-3) (1995).
79. Kim, G.-B., Yoon, S.-H., Kim, S.-S. & So, B.-D. Transition from buckling to subduction on strike-slip continental margins: Evidence from the east sea (Japan sea). *Geology* **46**, 603–606. <https://doi.org/10.1130/g40305.1> (2018).
80. Clark, P. U. et al. The last glacial maximum. *Science* **325**, 710–714. <https://doi.org/10.1126/science.1172873> (2009).
81. Lambeck, K., Yokoyama, Y. & Purcell, T. Into and out of the last glacial maximum: Sea-level change during oxygen isotope stages 3 and 2. *Quatern. Sci. Rev.* **21**, 343–360. [https://doi.org/10.1016/s0277-3791\(01\)00071-3](https://doi.org/10.1016/s0277-3791(01)00071-3) (2002).
82. Cathles, L., Su, Z. & Chen, D. The physics of gas chimney and pockmark formation, with implications for assessment of seafloor hazards and gas sequestration. *Mar. Pet. Geol.* **27**, 82–91. <https://doi.org/10.1016/j.marpetgeo.2009.09.010> (2010).

Acknowledgements

We appreciate SLB for providing the Petrel license and thank to KIGAM for providing the seismic data from Pohang, East sea. Also, the data in this study was provided by the Basic Research Project (24-3313) of the Korea Institute of Geoscience and Mineral Resources (KIGAM) funded by the Ministry of Science and ICT of Korea.

Author contributions

M. J. Lee conducted the data analysis & wrote the original manuscript. G.-B. Kim and Y. Shen built a geological scenario & performed seismic interpretation. J. Ha acquired the data, and Y. Cho supervised the research project and performed a comprehensive analysis of the dataset. All authors reviewed the manuscript.

Funding

This work is supported by Korea Institute of Energy Technology Evaluation and Planning (KETEP) grant funded by the Korea government, MOTIE: 20214000000500, Training program of CCUS for the green growth. Also, this work was partially supported by a grant from the Human Resources Development program (No. 20204010600250) of the Korea Institute of Energy Technology Evaluation and Planning (KETEP), funded by the Ministry of Trade, Industry, and Energy of the Korean Government.

Declarations

Competing interests

The authors declare no competing interests.

Additional information

Correspondence and requests for materials should be addressed to Y.C.

Reprints and permissions information is available at www.nature.com/reprints.

Publisher's note Springer Nature remains neutral with regard to jurisdictional claims in published maps and institutional affiliations.

Open Access This article is licensed under a Creative Commons Attribution-NonCommercial-NoDerivatives 4.0 International License, which permits any non-commercial use, sharing, distribution and reproduction in any medium or format, as long as you give appropriate credit to the original author(s) and the source, provide a link to the Creative Commons licence, and indicate if you modified the licensed material. You do not have permission under this licence to share adapted material derived from this article or parts of it. The images or other third party material in this article are included in the article's Creative Commons licence, unless indicated otherwise in a credit line to the material. If material is not included in the article's Creative Commons licence and your intended use is not permitted by statutory regulation or exceeds the permitted use, you will need to obtain permission directly from the copyright holder. To view a copy of this licence, visit <http://creativecommons.org/licenses/by-nc-nd/4.0/>.

© The Author(s) 2024